Journal of Power Sources 426 (2019) 143–150

Contents lists available at ScienceDirect

Journal of Power Sources

journal homepage: www.elsevier.com/locate/jpowsour

Sheet-type Li_6PS_5Cl-infiltrated Si anodes fabricated by solution process for all-solid-state lithium-ion batteries

Dong Hyeon Kim[a,b,1], Han Ah Lee[a,1], Yong Bae Song[a], Jun Woo Park[c], Sang-Min Lee[c], Yoon Seok Jung[a,*]

[a] Department of Energy Engineering, Hanyang University, Seoul, 04763, South Korea
[b] School of Energy and Chemical Engineering, Ulsan National Institute of Science and Technology, Ulsan, 44919, South Korea
[c] Battery Research Center, Korea Electrotechnology Research Institute, Changwon, 642-120, South Korea

HIGHLIGHTS

- Sheet-type Si electrodes are fabricated by infiltrating solution-processable SEs.
- Li_6PS_5Cl-infiltrated Si electrodes show high capacities of more than 3000 mA h g^{-1}.
- Effects of the Si size, binders, and pressure on the performances are investigated.
- $LiCoO_2$/Si full-cells showing high energy density (338 Wh kg^{-1}) are demonstrated.

GRAPHICAL ABSTRACT

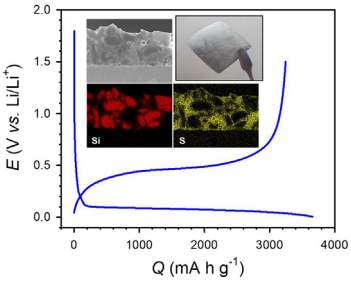

ARTICLE INFO

Keywords:
All-solid-state batteries
Silicon anodes
Solid electrolytes
Solution-process
Infiltration

ABSTRACT

All-solid-state lithium-ion batteries (ASLBs) employing sulfide solid electrolytes are considered a promising alternative to conventional lithium-ion batteries (LIBs) from the perspectives of safety and high energy density. From a practical point of view, the development of sheet-type electrodes employing alternative electrode materials by scalable fabrication is of prime importance. While Si has been extensively studied for next-generation LIBs, reports on ASLBs are scarce. Herein, we fabricate sheet-type Si composite electrodes by infiltrating conventional LIB electrodes with solid electrolytes using a homogeneous Li_6PS_5Cl-ethanol solution. Further, we systematically investigate effects of the particle size (micro- vs. nano-Si) and polymeric binders (polyvinylidene fluoride vs. polyacrylic acid/carboxymethyl cellulose) on the electrochemical performance of ASLBs under varying external pressures (140, 20, and 5 MPa) upon cycling. Owing to intimate ionic contacts enabled by liquefied solid electrolytes, the Li_6PS_5Cl-infiltrated Si electrodes show higher capacities of over 3000 mA h g^{-1} at 0.25 mA cm^{-2} and 30 °C as compared with conventional dry-mixed electrodes. At 20 MPa, the Si electrodes using micro-Si and polyvinylidene fluoride show marginal degradation of performance. The high energy density of 338 W h kg^{-1} of $LiCoO_2$/Si ASLBs fabricated using the Li_6PS_5Cl-infiltrated electrodes is demonstrated, highlighting the prospect of high-energy practical ASLBs.

* Corresponding author.
E-mail address: yoonsjung@hanyang.ac.kr (Y.S. Jung).
[1] These authors contributed equally.

https://doi.org/10.1016/j.jpowsour.2019.04.028
Received 16 January 2019; Received in revised form 28 March 2019; Accepted 7 April 2019

1. Introduction

Lithium-ion batteries (LIBs) are widely used in portable electronic devices owing to their high energy and power densities [1,2]. The ongoing interest in battery-driven electric vehicles (BEVs) has led to considerable progress in LIB technologies in terms of their energy density and long cycle life [2,3]. However, the safety problem originating from the use of flammable organic liquid electrolytes is a serious obstacle for their large-scale applications such as in BEVs and energy storage systems [4–6]. In this regard, all-solid-state lithium-ion batteries (ASLBs) employing nonflammable inorganic solid electrolytes (SEs) have emerged as a promising alternative to conventional LIBs owing to their better safety characteristics [4–9]. These batteries have the potential to surpass the energy density of LIBs in the pack level because inactive components could be substantially reduced owing to a reduced need for thermal management and the design of stacking bipolar electrodes [4,6,7,10]. Among the various SE materials, sulfide SEs are considered promising candidates because of their excellent deformability, which enables the formation of 2D ionic contacts by the mechanical sintering process (or cold pressing) [4,11,12]. Moreover, there has been remarkable progress in the Li-ion conductivity for sulfide SEs, which is comparable with that of liquid electrolytes (e.g., $Li_{10}GeP_2S_{12}$: 1.2×10^{-2} S cm^{-1}, $Li_{9.54}Si_{1.74}P_{1.44}S_{11.7}Cl_{0.3}$: 2.5×10^{-2} S cm^{-1}, $Li_7P_3S_{11}$: 1.7×10^{-2} S cm^{-1}, Li_6PS_5X (X = Cl, Br): $\geq 1.0 \times 10^{-3}$ S cm^{-1}) [6,13–15].

In most previous reports, the composite-structured bulk-type ASLBs employed pelletized electrodes prepared by cold pressing a mixture of active materials, SEs, and carbon additives in a dry condition [4,6,16]. However, the resulting mixture electrodes have poor mechanical properties to be scaled up. Sheet-type electrodes fabricated using polymeric binders are, therefore, required for practical applications [4,17–22]. Recently, our group reported pouch-type 80 × 60 mm^2 $LiNi_{0.6}Co_{0.2}Mn_{0.2}O_2$/graphite all-solid-state full cells using slurry-mixed electrodes, showing the cell-based energy density of 184 W h (kg of electrodes with current collectors and SE layers)$^{-1}$ and 432 W h L^{-1} [22]. Furthermore, our group reported a new scalable fabrication protocol for sheet-type ASLB electrodes using conventional polyvinylidene fluoride (PVDF)-based LIB electrodes by infiltration of solution-processable SEs of Li_6PS_5Cl (LPSCl, using ethanol) or 0.4LiI-0.6Li_4SnS_4 (using methanol) [18]. The infiltration of SE solutions allowed for favorable ionic contacts and percolations in the composite electrodes, resulting in high capacities of $LiCoO_2$ (LCO, 141 mA h g^{-1}) and graphite (364 mA h g^{-1}) electrodes. The high cell-based energy density of LCO/graphite full cells employing the SE-infiltrated electrodes (279 W h $kg_{LCO+graphite}^{-1}$) was achieved. However, the energy densities of ASLBs using the as-developed sheet-type electrodes are yet to be improved for competing with those for the conventional LIBs (max. ~260 W h kg^{-1} and ~683 W h L^{-1}, cell based) [23]. Significant improvements in energy density for ASLBs could be possible by replacing the conventional electrode materials with high-capacity alternative ones. Li metal is an ideal anode material owing to its high theoretical capacity (3860 mA h g^{-1}), low density (0.59 g cm^{-3}), and lowest potential (−3.04 V vs. SHE) [24–26]. Unfortunately, the penetrating growth of Li metals through the grain boundary and pores of SEs, which results in internal short circuits, is a serious challenge [10,27–29].

Si exhibits the highest specific capacity among alloying materials (4200 mA h g^{-1} for $Li_{4.4}Si$) and low operating voltage (~0.3 V vs. Li/Li$^+$) and is naturally abundant [30]. In this regard, Si could be a promising alternative anode material for ASLBs as the case for next-generation LIBs [30,31]. Despite its extremely high capacity, the practical application of Si for LIBs has been hindered by its huge volume changes (~400%) during lithiation and de-lithiation, which results in the pulverization of Si particles and loss of electrical contact in electrodes [30–32]. Many studies have been devoted to realizing the use of Si anodes for LIBs; reducing the particle (or domain) size [33,34], nanostructuring with buffering phases such as carbonaceous materials [33,35], providing void spaces to accommodate large volume changes [36–38]. Furthermore, the use of advanced polymeric binders, such as poly(acrylic acid) (PAA) [39], sodium carboxymethyl cellulose (CMC) [40], cross-linked PAA/CMC [41], and polyrotaxane incorporated PAA [42], showed significantly improved cycling performances of Si electrodes compared with the electrodes employing the conventional binder PVDF [41]. The underlying improvement mechanism is attributed to better adhesion between electrode components and the resilience of binders, which allow for maintaining electrical contacts during repeated volume changes of Si [43,44].

Despite the extensive efforts to develop Si anodes for conventional LIBs, to date only a few reports are available on Si anodes for ASLBs. Most of the results were based on dry-mixed electrodes using nano-sized Si with extremely low mass loadings (0.2–0.3 mg cm^{-2} of Si) or thin-film-type Si [45–48]. Moreover, it should be noted that Si electrodes for ASLBs were tested under high external pressures (50–100 MPa), which would affect the ionic/electronic contacts and thus their electrochemical performances [17,46,49,50].

Given the aforementioned backgrounds and motivations, herein, SE-infiltrated Si electrodes using solution-processable LPSCl are fabricated for ASLBs, and the effects of the particle size of Si (micro- or nano-Si), polymeric binders (PVDF or PAA/CMC), and external pressure (140 or 20 or 5 MPa) on their electrochemical performance are systematically investigated. The LPSCl-infiltrated Si electrodes show high reversible capacities of over 3000 mA h g^{-1} between 0.005 and 1.5 V (vs. Li/Li$^+$) at 30 °C, outperforming conventional dry-mixed electrodes. This performance is attributed to the excellent ionic contacts and percolation enabled by liquefied SEs. Finally, the LPSCl-infiltrated LCO/micro-Si (m-Si) all-solid-state full cells show a high energy density of 338 W h kg_{LCO+Si}^{-1}.

2. Experimental

2.1. Preparation of materials and electrodes

The argyrodite Li_6PS_5Cl (LPSCl) powders were prepared by mechanical milling of Li_2S (99.9%, Alfa Aesar), P_2S_5 (99%, Sigma-Aldrich), and LiCl (99.99%, Sigma-Aldrich) at 600 rpm for 10 h at room temperature with ZrO_2 balls, which are referred to as "BM-LPSCl." An LPSCl solution was then prepared by dissolving BM-LPSCl powders in anhydrous EtOH (99.5%, Sigma-Aldrich) at a concentration of 0.37 M. The solution-processed LPSCl powders, which are referred to as "sol-LPSCl," were synthesized by evaporating EtOH followed by heat treatment at 180 °C under vacuum. The conventional Si electrodes used for the infiltration of solution-processable SEs were fabricated by casting slurries on a Ni foil. The slurries were prepared by mixing Si, polymeric binder (PVDF (KF1100, Kureah Inc) or PAA/CMC (50/50 wt %, Aldrich)), and carbon additives (Super P) in the weight ratio of 80:10:10 in N-methyl pyrrolidinone (for PVDF) or water (for PAA/CMC) as solvent. Micro-Si (10 μm, Shandong) and nano-Si (< 50 nm, Alfa Aesar) were used. The mass loading of Si electrodes was 0.8–1.2 mg_{Si} cm^{-2}. The infiltration of LPSCl into conventional Si electrodes was carried out by dipping the Si electrodes in the LPSCl solution, followed by evaporation of the solvent in an Ar-filled glove box and subsequent heat treatment at 180 °C under vacuum. The LPSCl-infiltrated LCO electrode was prepared through the same procedure as in a previous paper [18]. The weight fraction of the infiltrated SEs was measured to be ~50 wt%. The Li_3PS_4 powders with a conductivity of 1.4×10^{-3} S cm^{-1} at 30 °C were prepared by mechanical milling of Li_2S and P_2S_5 at 500 rpm for 10 h with ZrO_2 balls at room temperature and subsequent heat treatment at 243 °C for 1 h in a glass ampoule under vacuum. The Mixture1 electrode was prepared by manual mixing of m-Si, sol-LPSCl, and Super P in a dry condition. The Mixture2 electrode was prepared by manual mixing of m-Si, sol-LPSCl, Super P, and PVDF in a dry condition. The composition of mixture electrodes was 40:50:5:(5) (m-Si:sol-LPSCl:Super P:(PVDF)).

2.2. Materials characterization

Raman spectra were measured with a 532 nm green laser using an NRS-3100 (JASCO). For X-ray powder diffraction (XRD) measurements, samples were sealed with a Be window and mounted on a MiniFlex600 diffractometer (Rigaku Corp.) (Cu K_α radiation of 1.54056 Å) at 15 mA and 40 kV. Cross sections of surfaces of the electrodes were prepared by polishing at 4 kV for 3 h with an Ar ion beam (JEOL, IB-19510CP). The field-emission scanning electron microscopy (FESEM) images and the corresponding energy-dispersive X-ray spectroscopy (EDXS) elemental maps of cross-sectioned electrodes were obtained using a JSM-7619FPlus (JEOL). For FESEM measurements, the SE-infiltrated Si electrodes were densified by pressing under 770 MPa at room temperature.

2.3. Electrochemical characterization

The Li-ion conductivity was measured by the alternating current (AC) impedance method using a Li-ion blocking Ti/SE/Ti cell. For electrochemical characterization, all-solid-state Si/SE/Li-In half cells were fabricated through the following procedure. $Li_{0.5}In$ prepared by mixing Li (FMC Lithium Corp.) and In (99%, Sigma-Aldrich) powders was used as the counter and reference electrode. The LPS powders (150 mg) were cold pressed to form an SE layer. Afterwards, the LPSCl-infiltrated Si electrodes or dry-mixed electrodes (Mixture1 or Mixture2) were put on one side of the SE layer. The $Li_{0.5}In$ electrodes were spread on the other side of the SE layer. Finally, the assembled Si/SE/Li-In was pressed at 770 MPa in a polyether ether ketone (PEEK) mold (13 mm of diameter) with Ti metal rods as current collectors. The galvanostatic charge-discharge cycling of the all-solid-state Si half cells was carried out in a voltage range of 0.005–1.5 V (vs. Li/Li^+) for the first cycle and 0.01–1.2 V (vs. Li/Li^+) for subsequent cycles at 30 °C. For self-discharge experiments, Si/Li-In half cells were cycled once and discharged to 0.01 V (vs. Li/Li^+). Then, the cells were kept for 7 days at 30 °C, followed by de-lithation (charge). The all-solid-state LCO/m-Si full cells were prepared by putting the SE-infiltrated LCO and m-Si electrodes on each side of the SE layer, followed by pressing at 770 MPa. The mass loading of LCO electrodes was 10 mg_{LCO} cm^{-2}. The $LiNbO_3$-coated LCO was used to minimize side reactions at LCO-LPSCl interfaces [16]. The *np* ratios (the areal capacity ratio of negative to positive electrodes) for LCO/Si full cells were ~1.7. The galvanostatic charge-discharge cycling of the all-solid-state LCO/Si cell was carried out in a voltage range of 2.8–4.2 V at 30 °C. An external pressure of 140 or 20 MPa was applied using cell holders (Fig. S1) during the operation of all-solid-state cells. Using the pressure monitoring sensor, the applied pressure was controlled by tightening the screws of the cell holders. The liquid-electrolyte cells using Li metal as the counter and reference electrode were tested using 2032-type coin cells. Prior to the assembly of coin cells, all the electrodes were heat treated at 180 °C under vacuum. A solution of 1.0 M $LiPF_6$ in a mixture of ethylene carbonate (EC) and diethyl carbonate (DEC) (1:1 *v/v*) with 10 wt% of fluoroethylene carbonate (FEC) was used as the electrolyte. A polypropylene (PP)/polyethylene (PE)/PP tri-layer film (Celgard Inc.) was used as the separator. The specific capacity shown is based on the mass of active materials.

3. Results and discussion

For the solution-processable SE, LPSCl powders prepared by mechanical milling of precursors Li_2S, P_2S_5, and LiCl, referred to as "BM-LPSCl," were completely dissolved in anhydrous EtOH. After evaporating the solvent under vacuum and the subsequent heat treatment at 180 °C under vacuum, LPSCl powders were recovered. These powders are referred to as "sol-LPSCl." The Nyquist plots of the as-obtained SEs using Li-ion blocking Ti/SE/Ti cells are shown in Fig. S2. The Li-ion conductivity of sol-LPSCl is approximately one order of magnitude lower (0.1 mS cm^{-1}) than that of BM-LPSCl (2.0 mS cm^{-1}), which

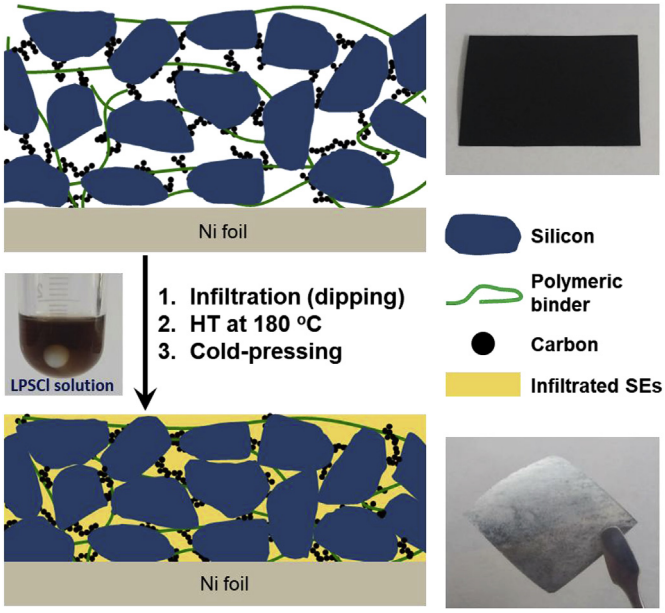

Fig. 1. Schematic diagram illustrating the process for infiltration of conventional Si composite electrodes with solution-processable SEs. The photographs show the m-Si electrodes before and after the infiltration of Li_6PS_5Cl (LPSCl). A photograph of LPSCl-dissolved ethanol solution is also shown.

stems from trace amounts of organic residues and/or low crystallinity [18]. The Raman spectra of the BM-LPSCl and sol-LPSCl reveal the characteristic peak for PS_4^{3-} (Fig. S3a). Also, the XRD patterns of BM-LPSCl and sol-LPSCl match the argyrodite Li_6PS_5Cl peaks (CIF No. 418490). However, for sol-LPSCl, trace amounts of impurities such as α-Li_3PS_4, Li_2S, and LiCl are shown (Fig. S3b), which would also account for the lower Li-ion conductivity of sol-LPSCl than that of BM-LPSCl or solid-state synthesized LPSCl prepared at high temperature [18,51].

The process of infiltration of solution-processable SEs into conventional composite Si electrodes is shown in Fig. 1. The Si composite electrodes were fabricated by casting slurries, which were a mixture of active materials (m-Si (~10 μm) or nano-sized Si (n-Si, ~50 nm)), polymeric binder (PVDF or PAA/CMC), and carbon additives. The infiltration of the LPSCl solution was carried out by a dip-coating method, followed by the removal of solvent and subsequent heat treatment at 180 °C under vacuum. As the surfaces of Si in the composite electrodes were wetted by the SE solution, they could be well covered with an LPSCl layer. The weight fraction of LPSCl was ~50 wt% after infiltration. Finally, the LPSCl-infiltrated Si electrodes were densified by cold pressing under 770 MPa.

In an attempt to examine the compatibility of Si and LPSCl solutions, Raman and XRD analyses were performed for the m-Si electrodes before and after the SE-infiltration (Fig. 2a and b). The LPSCl-infiltrated Si electrode shows strong peaks at 520 cm^{-1} (labeled "#"), which originate from the T_{2g} mode of crystalline Si [52]. The LPSCl peak, centered at 423 cm^{-1} and corresponding to PS_4^{3-}, is also obtained in an LPSCl-infiltrated electrode, which is consistent with the Raman spectrum of sol-LPSCl (Fig. S3a). The XRD patterns of the LPSCl-infiltrated electrode reveal no change in the peak position for Si (labeled "#") and include the signature peaks for LPSCl (Figs. 2b and S4). The impurities for sol-LPSCl are not clearly seen in the composite electrodes owing to the limited mass loading of LPSCl in the composite electrodes. Both the Raman and XRD results indicate a negligible chemical interaction between Si and the LPSCl solution and confirm that the formation of LPSCl is not affected by electrode components even after heat treatment at 180 °C.

Fig. 2c shows the cross-sectional FESEM image of the cold-pressed LPSCl-infiltrated m-Si electrode and its corresponding EDXS elemental

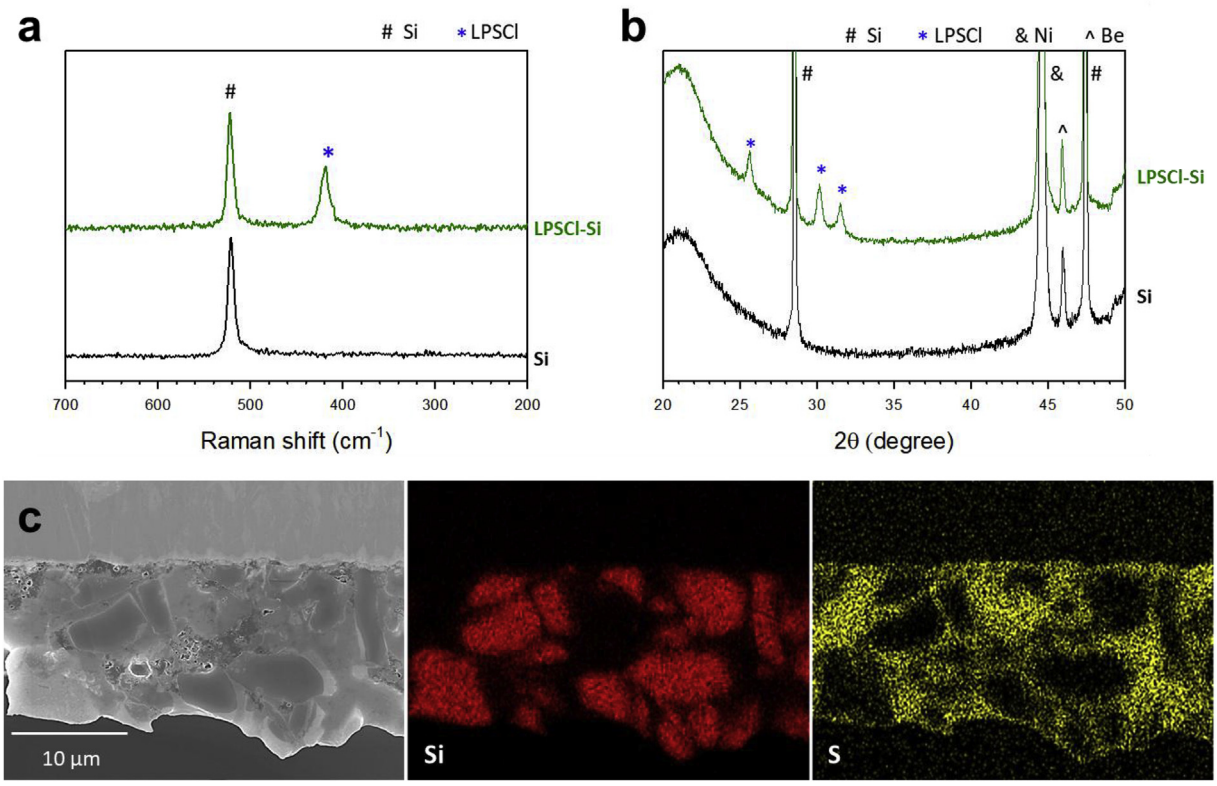

Fig. 2. Characterization of the LPSCl-infiltrated m-Si electrodes: (a) Raman spectra, (b) XRD patterns of m-Si electrodes before and after the infiltration of solution-processed LPSCl, and (c) cross-sectional FESEM image of the LPSCl-infiltrated m-Si electrode and its corresponding EDXS elemental maps.

maps of silicon and sulfur. The pores of the m-Si electrode are filled well with LPSCl, which is attributed to the excellent wettability of the LPSCl solution on the electrode and the high deformability of the sulfide SEs. Moreover, negligible porosity is observed after cold pressing, which confirms the intimate contact between m-Si and LPSCl. The cross-sectional FESEM image of the LPSCl infiltrated n-Si electrode and its corresponding EDXS elemental maps also show an even distribution of LPSCl in the electrode, confirming the excellent penetration of the LPSCl solution into electrodes using the nanoparticles (Fig. S5).

The electrochemical characterization of LPSCl-infiltrated Si electrodes employing two different sized Si (m-Si or n-Si) with two different kinds of binders (PVDF or PAA/CMC) was carried out using all-solid-state Si/Li-In half cells at 0.05C (0.20–0.25 mA cm^{-2}) and 30 °C under an external pressure of 140 MPa. The first and second discharge-charge voltage profiles of LPSCl-infiltrated Si electrodes are shown in Fig. 3a (m-Si) and 3b (n-Si). Two features are worth noting. First, high first-cycle charge capacities of over 3000 mA h g^{-1} and initial Coulombic efficiencies (CEs) of over 80% are obtained for both n-Si and m-Si. In a previous report on binder-free Si composite electrodes, a similar performance was achieved [53]. In conventional LIBs, it is typical that m-Si electrodes show much lower reversible capacities and initial CEs than those of the n-Si electrodes because the loss of electrical contact is more severe for m-Si than for n-Si owing to larger absolute volume changes in m-Si than that of n-Si [30,33,34]. In this work, the m-Si electrode shows the higher initial CE of 88.7% as compared with that of the n-Si electrode (80.4%). Notably, this value (88.7%) is higher than that for the m-Si electrode with PAA/CMC using FEC-added liquid electrolytes (84.4%, Fig. S6). The lower initial CE for the n-Si electrode than that for the m-Si electrode originates from more severe irreversible consumption of Li [53]. However, after the 10th cycle, the CEs remain to show ≥ ~99.5% for both electrodes, indicating the favorable passivating layers formed at initial cycles (Fig. S7). Second, in contrast to the conventional Si electrodes for LIBs, effects of polymeric binders (PVDF vs. PAA/CMC) appear to be marginal for ASLBs. The electrochemical performances of m-Si for all-solid-state cells and liquid-electrolyte cells are compared in Fig. S6. For liquid-electrolyte cells, whereas the discharge (lithiation) capacities for the m-Si electrodes using PVDF and PAA/CMC are similar, the charge (de-lithiation) capacity for the electrode using PAA/CMC is higher (~2250 mA h g^{-1}) than that using PVDF (~890 mA h g^{-1}). It is known that, during the heat-treatment step for preparing the electrodes using PAA and CMC, cross-linking of PAA and CMC forms a three-dimensionally connected polymeric backbone, thereby helping to keep the electrical contacts between electrode components upon large volume changes [41]. In this regard, the irrelevance of polymeric binders on the performance of all-solid-state cells could be surprising. For all-solid-state cells, it should be noted that a high external pressure (140 MPa) was applied during the operation of the cells, which could force to maintain the mechanical integrity of the electrode components. Even a higher charge capacity of Si in all-solid-state cells (~3246 mA h g^{-1}) than those in liquid-electrolyte cells could be thus attributed to the high external pressure. In short, pressuring the all-solid-state cells under operation could be effective for maintaining ionic and electronic contacts during lithiation and de-lithiation of Si, and nullifies the effects of the particle size of Si and polymeric binders.

The differential discharge-charge voltage profiles at first two cycles for the m-Si and n-Si electrodes are plotted in Fig. 3e and f. The presence of the sharp single peak only for m-Si at ~0.45 V (vs. Li/Li^+) on the first de-lithiation is indicative of the formation of the crystalline $Li_{15}Si_4$ phase during the precedent lithiation process below 50 mV (vs. Li/Li^+) at the initial cycle in crystalline bulk Si [32].

The charge capacities of the LPSCl-infiltrated Si electrodes varying by different C-rates as a function of the cycle number are shown in Fig. 3c and d. The rate capabilities of Si electrodes do not show significant variations by the binders (PVDF vs. PAA/CMC) or the size of Si (m-Si vs. n-Si). The rate-determining step in the all-solid-sate cells is considered to be Li^+ transport in SEs, especially in the thick SE layers (~1 mS cm^{-1} and 600-μm thick) rather than that in Si particles

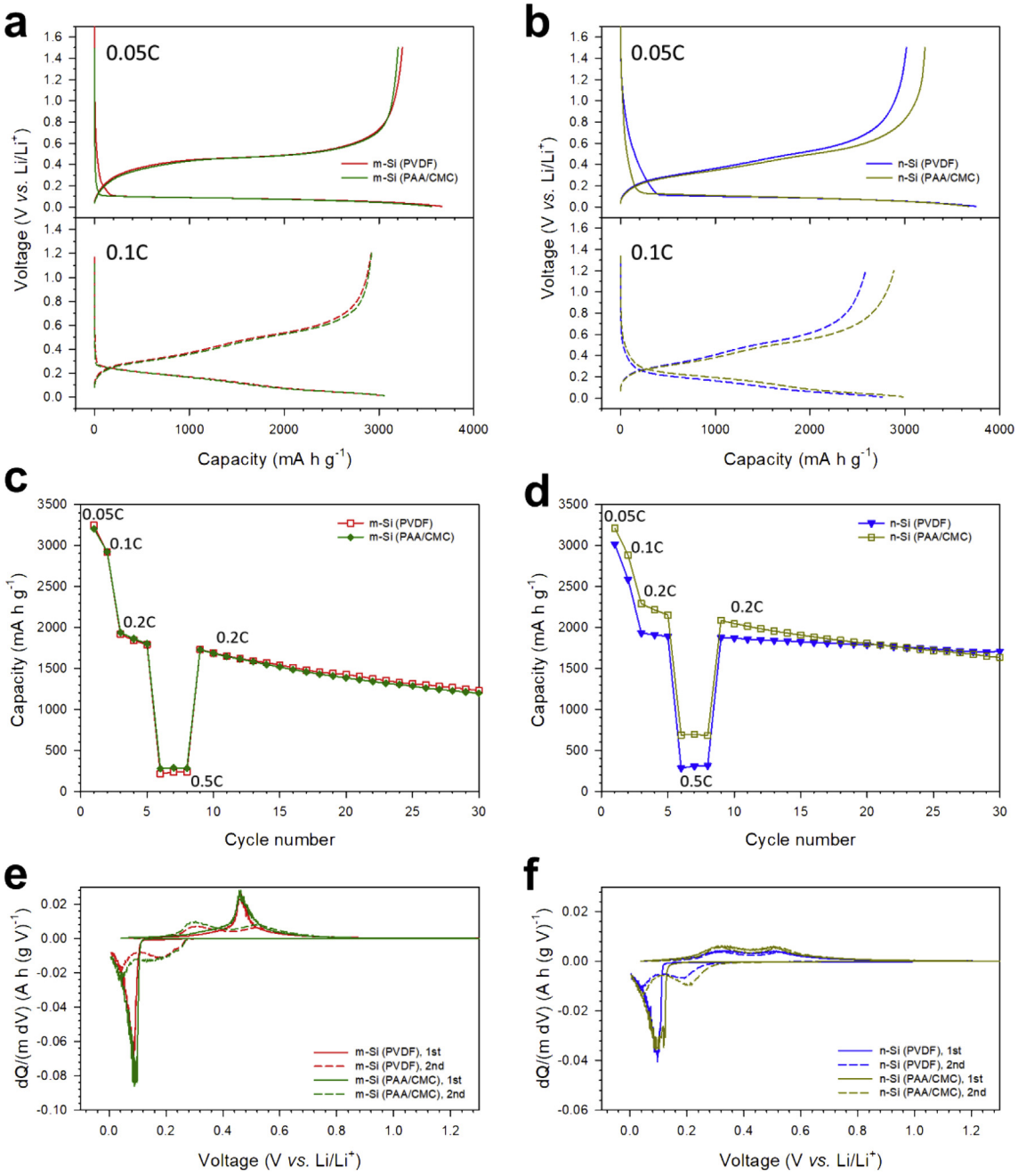

Fig. 3. Electrochemical characterization of all-solid-state Si/Li-In half cells employing LPSCl-infiltrated electrodes at 30 °C. First- and second-cycle discharge-charge voltage profiles of (a) m-Si and (b) n-Si electrodes (0.005–1.5 V for the first cycle and 0.01–1.2 V for the second cycle). Charge capacity varied by C-rate as a function of cycle number for (c) m-Si and (d) n-Si electrodes in all-solid-state cells. The C-rates for charge and discharge were the same (1C = 4.0–5.0 mA cm^{-2}). The differential discharge-charge capacity profiles during the first two cycles for (e) m-Si and (f) n-Si electrodes.

[11,54,55]. The cycling performances of n-Si are slightly superior to those of m-Si. The capacity retention of n-Si as compared with the capacity at the 9th cycle after 30 cycles is higher (91.1% and 78.2% for using PVDF and PAA/CMC, respectively) than that of m-Si (73.9% and 69.3% for using PVDF and PAA/CMC, respectively).

In Fig. 4, the electrochemical performance of the LPSCl-infiltrated m-Si electrode is compared with those of conventional dry-mixed electrodes without binders (referred to as “Mixture1”) and with PVDF binder (referred to as “Mixture2”). The LPSCl-infiltrated electrode shows much higher charge capacity (3246 mA h g^{-1}) than those for Mixture1 (1437 mA h g^{-1}) and Mixture2 (1243 mA h g^{-1}) electrodes, which is primarily attributed to more intimate contact of Si with LPSCl enabled by the liquefied SEs [11,12]. Also, the manual mixing of three or four components (Si, SEs, carbon additives, (binders)) is limiting in achieving favorable or optimal electronic and ionic conduction pathways at the same time. Further improvement of the performance might be possible by elaborating the mixture electrodes. However, it means more engineering effort, which could translate into more cost from a viability point of view. Thus, the superior performance of the SE-infiltrated Si electrodes to those of the conventional mixture electrodes highlights the unique advantages of the SE-infiltration protocol in terms of electrochemical performance and practical application [18].

Despite the high capacities of over 3000 mA h g^{-1}, the gradual capacity decay of the LPSCl-infiltrated Si electrodes (Fig. 3c and d or 4b) needs to be clarified. A possible side reaction between Si and LPSCl at a low voltage may cause an increase in the cell impedance. Fig. 5a

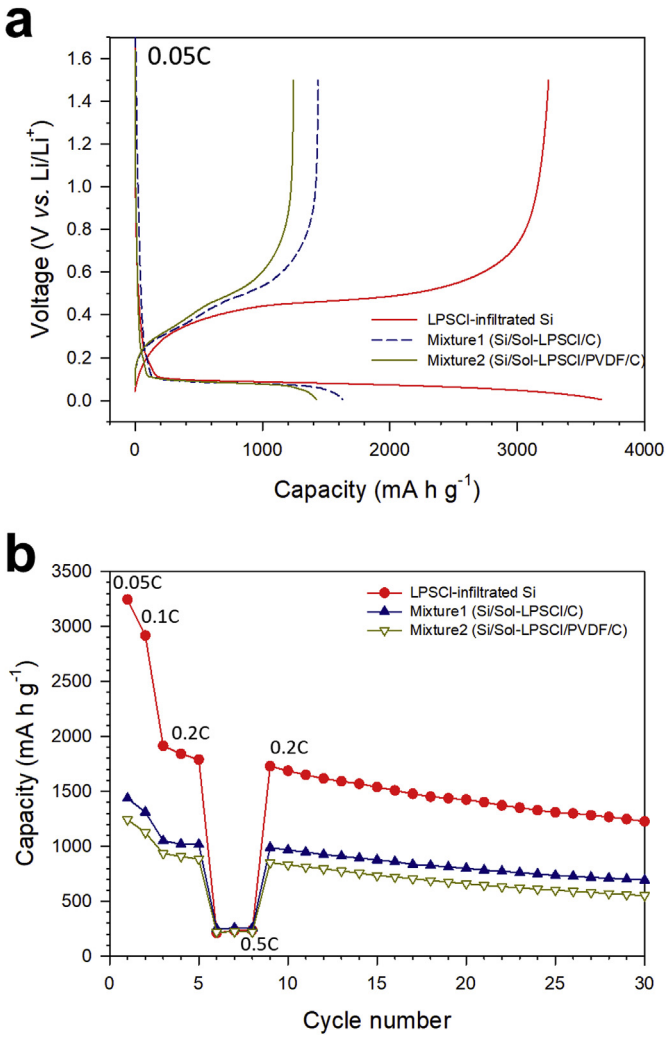

Fig. 4. Electrochemical performances of all-solid-state Si/Li-In half cells employing the LPSCl-infiltrated electrode and the conventional mixture electrodes, which were prepared by manual mixing in dry conditions (Mixture1 and Mixture2). (a) First-cycle discharge-charge voltage profiles of Si/Li-In all-solid-state cells at 0.05C (0.20–0.25 mA cm^{-2}) and 30 °C. (b) Rate performance of all-solid-state Si/Li-In cells.

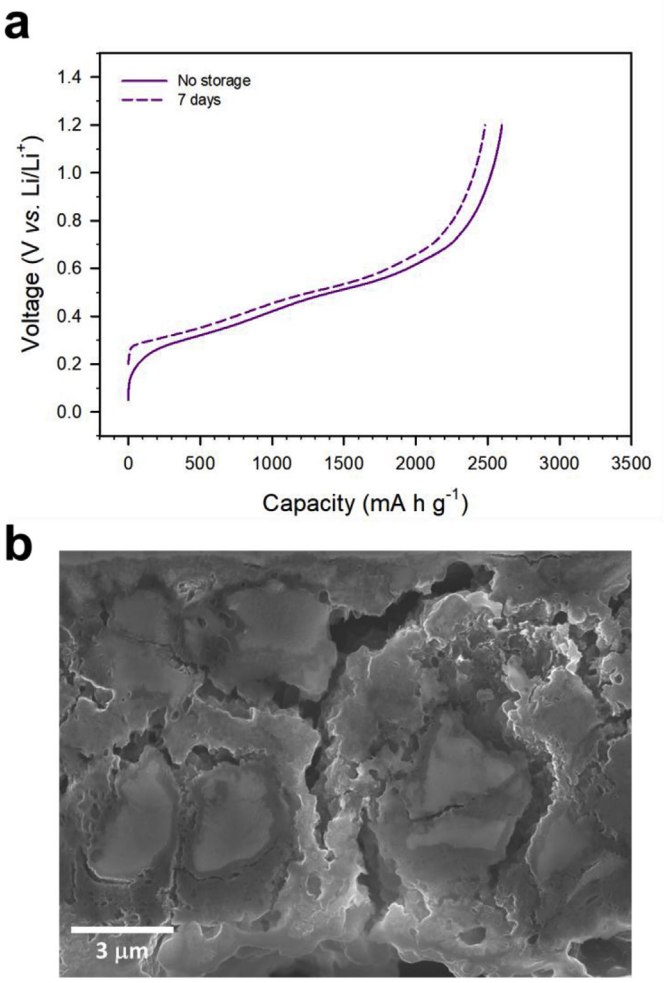

Fig. 5. (a) Charge (de-lithiation) voltage profiles of LPSCl-infiltrated n-Si electrode with variation of storage after discharge (lithiation) at 30 °C. (b) The cross-sectional FESEM image of the LPSCl-infiltrated m-Si electrode after 40 cycles.

compares the self-discharge behaviors of the LPSCl-infiltrated n-Si electrodes on varying the storage after lithiation (discharge) at 30 °C. The n-Si electrode was used owing to its higher surface area. While a marginal decrease in capacity is observed, the CE remains similar after storage for 7 days (97.4% vs. 97.0% without storage). Therefore, the capacity fading of Si by any side reaction between Li_xSi and LPSCl could be marginal. The cross-sectional FESEM image of m-Si electrodes after 40 cycles is shown in Fig. 5b. Compared with the fresh densified electrode (Fig. 2c), cracks are formed in the cycled electrodes, which must be caused by severe volume changes in Si during lithiation and de-lithiation. The corresponding ionic and electronic contact loss in the electrodes should be responsible for the gradual capacity fading in the Si electrodes. It is noted that the external pressure of 140 MPa is high enough to nullify the effects of the particle size of Si (m-Si vs. n-Si) and the polymeric binders (PVDF vs. PAA/CMC), but it could not heal the mechanical failure completely. In this study, a high external pressure of 140 MPa was applied using the lab-scale pelletized cells, illustrated in Fig. S1. However, it might not be feasible for large-scale ASLBs for practical applications [22,54,56].

In this regard, the effects of external pressure on the electrochemical performance of the SE-infiltrated Si electrodes for all-solid-state cells were assessed. The reversible capacities of LPSCl-infiltrated Si electrodes at different current densities with two different external pressures (140 and 20 MPa) are shown in Fig. 6, S8. Notably, the LPSCl-infiltrated Si electrodes exhibit similar capacities at both high (140 MPa) and low (20 MPa) external pressures regardless of the particle size and polymeric binders. The differences in capacities on varying the external pressure are considered within the ranges of experimental errors. Further lowering of the external pressure to 5 MPa for n-Si electrode results in the significantly lowered CE (80.4% and 82.2% under 140 and 20 MPa, respectively vs. 64.0% under 5 MPa, Fig. S9), indicating that the low external pressure of 5 MPa would be not enough to nullify the effects of large volume changes of Si during lithiation and de-lithiation. Although an in-depth analysis of mechano-electrochemistry of these Si-based all-solid-state cells and the corresponding design is required [49,50], a positive aspect of this result is that alternative high-capacity electrode materials could be enabled by engineering of external pressure. In contrast, for conventional LIBs using liquid electrolytes, possible mechanical failure of separators causing internal short circuit and leakage of electrolytes as well as severe degradation of performances restrict the external pressure to be low [56–59].

Finally, all-solid-state LCO/m-Si full cells employing the LPSCl-infiltrated LCO and m-Si electrodes (using PVDF) were tested at 30 °C (Fig. 7). The m-Si electrode was selected for the full cells because of its higher initial CE and tap density compared with the n-Si electrode. The

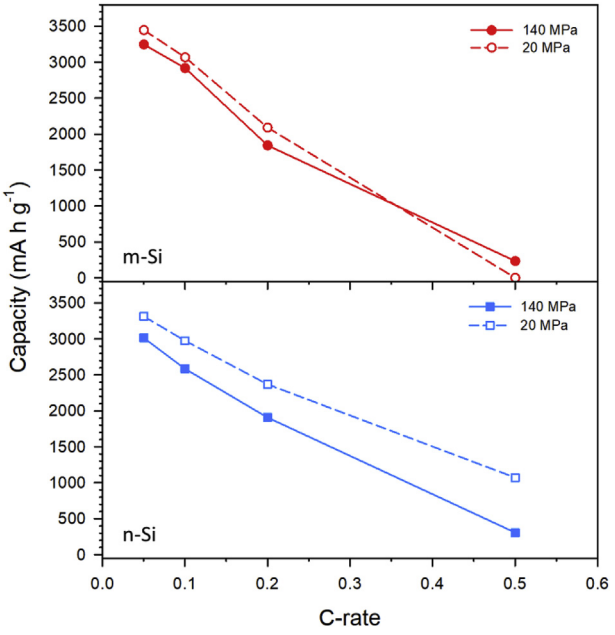

Fig. 6. Charge capacities for all-solid-state Si/Li-In cells employing LPSCl-infiltrated Si (m-Si or n-Si) electrodes operated under different external pressures, varied by C-rate at 30 °C. The PVDF was used as a binder.

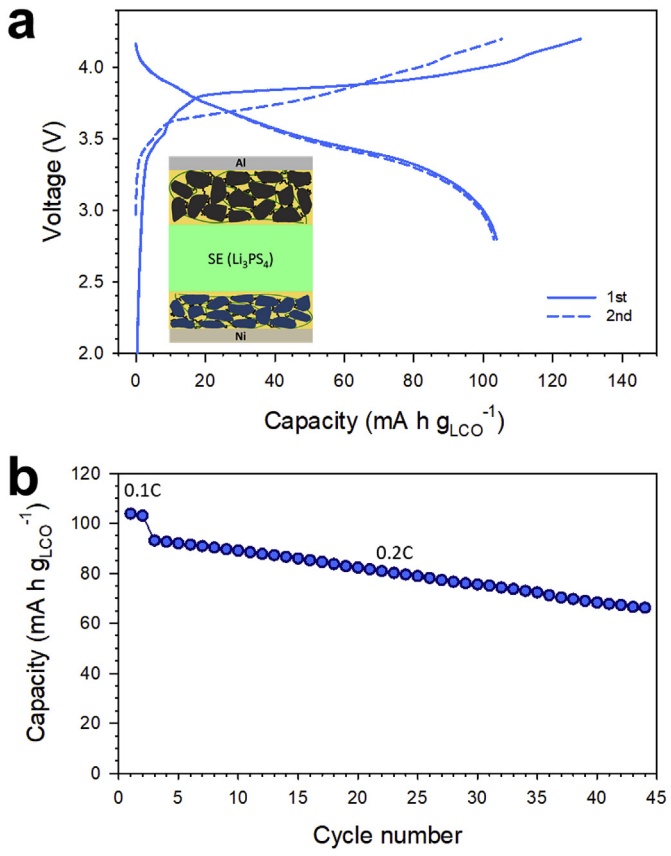

Fig. 7. Electrochemical performance of LCO/m-Si all-solid-state full-cells employing LPSCl-infiltrated LCO and m-Si electrodes at 30 °C: (a) Initial charge-discharge voltage profiles at 0.1C (0.14 mA cm^{-2}) and (b) cycling performance. The cell configuration of LCO/m-Si ASLBs is illustrated in the inset in (a).

LPSCl-infiltrated LCO electrode prepared using the same procedure as in our previous work was used as the cathode [18]. The full-cell configuration is shown in the inset in Fig. 7a. The LCO/m-Si ASLBs show a reversible capacity of 104 mA h g_{LCO}^{-1} at 0.14 mA cm^{-2} in the voltage range of 2.8–4.2 V, which translates into an energy density of 338 W h kg_{LCO+Si}^{-1}. The application of the high-capacity Si electrode increases the energy density by 21% compared with the LCO/graphite full cell (279 Wh kg_{LCO+Gr}^{-1}) in our previous report [18]. Furthermore, the LCO/m-Si full cell shows a promising cycling performance at 0.2C (0.28 mA cm^{-2}). Although their electrochemical performance is not excellent, further elaboration, such as using advanced Si materials [60], functional binders with Li^+ conductivity and/or self-healing ability [61,62], and advanced SE materials with favorable mechanical properties [11,63], combined with engineering of external pressure would lead to more improvements.

4. Conclusions

In summary, the sheet-type Si composite electrodes for ASLBs were fabricated by the infiltration of conventional LIB electrodes with solution-processable SEs (LPSCl). The liquefied LPSCl solution was compatible with Si and solidified on the surfaces of Si, allowing for the intimate ionic contact and favorable ionic pathways in the composite electrodes. The LPSCl-infiltrated Si electrodes showed much higher reversible capacities of over 3000 mA h g^{-1} at 30 °C when compared with those for the conventional dry-mixed electrodes. In contrast to the Si electrodes for LIBs using liquid electrolytes, the use of bulk Si (m-Si vs. n-Si) and PVDF (vs. PAA/CMC) did not considerably degrade the electrochemical performance for all-solid-state cells, which was attributed to the capability of applying the high external pressure during their operation. The slight capacity degradation was associated with the inevitable loss of contact upon volume changes of Si. Lowering the pressure from 140 to 20 MPa resulted in marginal degradation in the performance, providing a prospect in pressure engineering of alternative electrode materials for ASLBs. Finally, all-solid-state LCO/Si full cells using LPSCl-infiltrated LCO and m-Si electrodes successfully demonstrated a high energy density of 338 Wh kg_{LCO+Si}^{-1} at 0.14 mA cm^{-2} and 30 °C.

Acknowledgements

This work was supported by the KERI Primary research program of MSIP / NST (grant no. 18-12-N0101-20) and by the research fund of Hanyang University (grant no. HY-2018).

Appendix A. Supplementary data

Supplementary data to this article can be found online at https://doi.org/10.1016/j.jpowsour.2019.04.028.

References

[1] J.B. Goodenough, Y. Kim, Chem. Mater. 22 (2010) 587.
[2] M. Li, J. Lu, Z. Chen, K. Amine, Adv. Mater. (2018) 1800561.
[3] J.W. Choi, D. Aurbach, Nat. Rev. Mater. 1 (2016) 16013.
[4] K.H. Park, Q. Bai, D.H. Kim, D.Y. Oh, Y. Zhu, Y. Mo, Y.S. Jung, Adv. Energy Mater. (2018) 1800035.
[5] J. Kalhoff, G.G. Eshetu, D. Bresser, S. Passerini, ChemSusChem 8 (2015) 2154.
[6] Y. Kato, S. Hori, T. Saito, K. Suzuki, M. Hirayama, A. Mitsui, M. Yonemura, H. Iba, R. Kanno, Nat. Energy 1 (2016) 16030.
[7] K. Kerman, A. Luntz, V. Viswanathan, Y.-M. Chiang, Z. Chen, J. Electrochem. Soc. 164 (2017) A1731.
[8] J. Janek, W.G. Zeier, Nat. Energy 1 (2016) 16141.
[9] Z. Zhang, Y. Shao, B. Lotsch, Y.-S. Hu, H. Li, J. Janek, L.F. Nazar, C. Nan, J. Maier, M. Armand, L. Chen, Energy Environ. Sci. 11 (2018) 1945.
[10] Y.S. Jung, D.Y. Oh, Y.J. Nam, K.H. Park, Isr. J. Chem. 55 (2015) 472.
[11] K.H. Park, D.Y. Oh, Y.E. Choi, Y.J. Nam, L. Han, J.Y. Kim, H. Xin, F. Lin, S.M. Oh, Y.S. Jung, Adv. Mater. 28 (2016) 1874.
[12] A. Banerjee, K.H. Park, J.W. Heo, Y.J. Nam, C.K. Moon, S.M. Oh, S.T. Hong, Y.S. Jung, Angew. Chem. Int. Ed. 55 (2016) 9634.
[13] N. Kamaya, K. Homma, Y. Yamakawa, M. Hirayama, R. Kanno, M. Yonemura, T. Kamiyama, Y. Kato, S. Hama, K. Kawamoto, A. Mitsui, Nat. Mater. 10 (2011) 682.
[14] Y. Seino, T. Ota, K. Takada, A. Hayashi, M. Tatsumisago, Energy Environ. Sci. 7

(2014) 627.
[15] H.J. Deiseroth, S.T. Kong, H. Eckert, J. Vannahme, C. Reiner, T. Zaiss, M. Schlosser, Angew. Chem. Int. Ed. 47 (2008) 755.
[16] S.H. Jung, K. Oh, Y.J. Nam, D.Y. Oh, P. Brüner, K. Kang, Y.S. Jung, Chem. Mater. 30 (2018) 8190.
[17] S. Ito, S. Fujiki, T. Yamada, Y. Aihara, Y. Park, T.Y. Kim, S.-W. Baek, J.-M. Lee, S. Doo, N. Machida, J. Power Sources 248 (2014) 943.
[18] D.H. Kim, D.Y. Oh, K.H. Park, Y.E. Choi, Y.J. Nam, H.A. Lee, S.M. Lee, Y.S. Jung, Nano Lett. 17 (2017) 3013.
[19] D.Y. Oh, D.H. Kim, S.H. Jung, J.-G. Han, N.-S. Choi, Y.S. Jung, J. Mater. Chem. A 5 (2017) 20771.
[20] K. Lee, S. Kim, J. Park, S.H. Park, A. Coskun, D.S. Jung, W. Cho, J.W. Choi, J. Electrochem. Soc. 164 (2017) A2075.
[21] A. Sakuda, K. Kuratani, M. Yamamoto, M. Takahashi, T. Takeuchi, H. Kobayashi, J. Electrochem. Soc. 164 (2017) A2474.
[22] Y.J. Nam, D.Y. Oh, S.H. Jung, Y.S. Jung, J. Power Sources 375 (2018) 93.
[23] R. Schmuch, R. Wagner, G. Hörpel, T. Placke, M. Winter, Nat. Energy 3 (2018) 267.
[24] W. Xu, J. Wang, F. Ding, X. Chen, E. Nasybulin, Y. Zhang, J.-G. Zhang, Energy Environ. Sci. 7 (2014) 513.
[25] X.-B. Cheng, R. Zhang, C.-Z. Zhao, Q. Zhang, Chem. Rev. 117 (2017) 10403.
[26] S. Xin, Y. You, S. Wang, H.C. Gao, Y.X. Yin, Y.G. Guo, ACS Energy Lett. 2 (2017) 1385.
[27] L. Porz, T. Swamy, B.W. Sheldon, D. Rettenwander, T. Frömling, H.L. Thaman, S. Berendts, R. Uecker, W.C. Carter, Y.M. Chiang, Adv. Energy Mater. 7 (2017) 1701003.
[28] E.J. Cheng, A. Sharafi, J. Sakamoto, Electrochim. Acta 223 (2017) 85.
[29] Y.J. Nam, K.H. Park, D.Y. Oh, W.H. An, Y.S. Jung, J. Mater. Chem. A 6 (2018) 14867.
[30] M.T. McDowell, S.W. Lee, W.D. Nix, Y. Cui, Adv. Mater. 25 (2013) 4966.
[31] K. Feng, M. Li, W. Liu, A.G. Kashkooli, X. Xiao, M. Cai, Z. Chen, Small 14 (2018) 1702737.
[32] T. Hatchard, J. Dahn, J. Electrochem. Soc. 151 (2004) A838.
[33] Y.S. Jung, K.T. Lee, S.M. Oh, Electrochim. Acta 52 (2007) 7061.
[34] C.K. Chan, H. Peng, G. Liu, K. McIlwrath, X.F. Zhang, R.A. Huggins, Y. Cui, Nat. Nanotechnol. 3 (2008) 31.
[35] S.H. Ng, J. Wang, D. Wexler, K. Konstantinov, Z.P. Guo, H.K. Liu, Angew. Chem. Int. Ed. 118 (2006) 7050.
[36] K.T. Lee, Y.S. Jung, S.M. Oh, J. Am. Chem. Soc. 125 (2003) 5652.
[37] Y. Yao, M.T. McDowell, I. Ryu, H. Wu, N. Liu, L. Hu, W.D. Nix, Y. Cui, Nano Lett. 11 (2011) 2949.
[38] X. Li, P. Meduri, X. Chen, W. Qi, M.H. Engelhard, W. Xu, F. Ding, J. Xiao, W. Wang, C. Wang, J. Mater. Chem. 22 (2012) 11014.
[39] A. Magasinski, B. Zdyrko, I. Kovalenko, B. Hertzberg, R. Burtovyy, C.F. Huebner, T.F. Fuller, I. Luzinov, G. Yushin, ACS Appl. Mater. Interfaces 2 (2010) 3004.
[40] J. Li, R. Lewis, J. Dahn, Electrochem. Solid State Lett. 10 (2007) A17.
[41] B. Koo, H. Kim, Y. Cho, K.T. Lee, N.S. Choi, J. Cho, Angew. Chem. Int. Ed. 51 (2012) 8762.
[42] S. Choi, T.-w. Kwon, A. Coskun, J.W. Choi, Science 357 (2017) 279.
[43] T.-w. Kwon, J.W. Choi, A. Coskun, Chem. Soc. Rev. 47 (2018) 2145.
[44] H. Chen, M. Ling, L. Hencz, H.Y. Ling, G. Li, Z. Lin, G. Liu, S. Zhang, Chem. Rev. 118 (2018) 8936.
[45] J.E. Trevey, K.W. Rason, C.R. Stoldt, S.-H. Lee, Electrochem. Solid State Lett. 13 (2010) A154.
[46] D.M. Piper, T.A. Yersak, S.-H. Lee, J. Electrochem. Soc. 160 (2013) A77.
[47] R.B. Cervera, N. Suzuki, T. Ohnishi, M. Osada, K. Mitsuishi, T. Kambara, K. Takada, Energy Environ. Sci. 7 (2014) 662.
[48] J. Sakabe, N. Ohta, T. Ohnishi, K. Mitsuishi, K. Takada, Commun. Chem. 1 (2018) 24.
[49] W. Zhang, D. Schroeder, T. Arlt, I. Manke, R. Koerver, R. Pinedo, D.A. Weber, J. Sann, W.G. Zeier, J. Janek, J. Mater. Chem. A 5 (2017) 9929.
[50] R. Koerver, W. Zhang, L. de Biasi, S. Schweidler, A.O. Kondrakov, S. Kolling, T. Brezesinski, P. Hartmann, W.G. Zeier, J. Janek, Energy Environ. Sci. 11 (2018) 2142.
[51] S. Yubuchi, M. Uematsu, C. Hotehama, A. Sakuda, A. Hayashi, M. Tatsumisago, J. Mater. Chem. A 7 (2019) 558.
[52] D. Bermejo, M. Cardona, J. Non-Cryst. Solids 32 (1979) 405.
[53] M. Yamamoto, Y. Terauchi, A. Sakuda, M. Takahashi, J. Power Sources 402 (2018) 506.
[54] Y.J. Nam, S.-J. Cho, D.Y. Oh, J.-M. Lim, S.Y. Kim, J.H. Song, Y.-G. Lee, S.-Y. Lee, Y.S. Jung, Nano Lett. 15 (2015) 3317.
[55] B.R. Shin, Y.J. Nam, D.Y. Oh, D.H. Kim, J.W. Kim, Y.S. Jung, Electrochim. Acta 146 (2014) 395.
[56] J. Cannarella, C.B. Arnold, J. Power Sources 245 (2014) 745.
[57] E. Sahraei, R. Hill, T. Wierzbicki, J. Power Sources 201 (2012) 307.
[58] C. Peabody, C.B. Arnold, J. Power Sources 196 (2011) 8147.
[59] S. Abada, G. Marlair, A. Lecocq, M. Petit, V. Sauvant-Moynot, F. Huet, J. Power Sources 306 (2016) 178.
[60] Y. Jin, B. Zhu, Z. Lu, N. Liu, J. Zhu, Adv. Energy Mater. 7 (2017) 1700715.
[61] D.Y. Oh, Y.J. Nam, K.H. Park, S.H. Jung, K.T. Kim, A.R. Ha, Y.S. Jung, Adv. Energy Mater. (2019) 1802927.
[62] A. Kato, M. Yamamoto, A. Sakuda, A. Hayashi, M. Tatsumisago, ACS Appl. Energy Mater. 3 (2018) 1002.
[63] J.M. Whiteley, P. Taynton, W. Zhang, S.-H. Lee, Adv. Mater. 27 (2015) 6922.